

## 1 Pressure-Driven Metallization in Hafnium Diselenide

2 Adrián Andrada-Chacón,\* Ángel Morales-García, Miguel A. Salvadó, Pilar Pertierra, Ruth Franco,  
 3 Gastón Garbarino, Mercedes Taravillo, José A. Barreda-Argüeso, Jesús González, Valentín G. Baonza,  
 4 Jose Manuel Recio, and Javier Sánchez-Benítez



Cite This: <https://dx.doi.org/10.1021/acs.inorgchem.0c03223>



Read Online

ACCESS |



Metrics & More

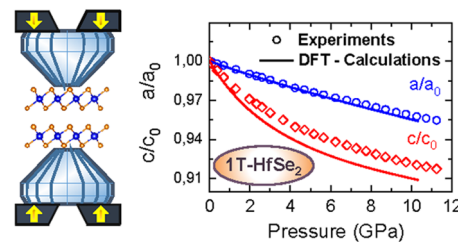


Article Recommendations



Supporting Information

5 **ABSTRACT:** The quest for new transition metal dichalcogenides (TMDs) with  
 6 outstanding electronic properties operating under ambient conditions draws us to  
 7 investigate the 1T-HfSe<sub>2</sub> polytype under hydrostatic pressure. Diamond anvil cell  
 8 (DAC) devices coupled to *in situ* synchrotron X-ray, Raman, and optical (vis–  
 9 NIR) absorption experiments along with density functional theory (DFT)-based  
 10 calculations prove that (i) bulk 1T-HfSe<sub>2</sub> exhibits strong structural and vibrational  
 11 anisotropies, being the interlayer direction especially sensitive to pressure changes,  
 12 (ii) the indirect gap of 1T-HfSe<sub>2</sub> trend to vanish by a  $-0.1$  eV/GPa pressure rate,  
 13 slightly faster than MoS<sub>2</sub> or WS<sub>2</sub>, (iii) the onset of the metallic behavior appears at  
 14  $P_{\text{met}} \sim 10$  GPa, which is to date the lowest pressure among common TMDs, and  
 15 finally, (iv) the electronic transition is explained by the bulk modulus  $B_0$ - $P_{\text{met}}$  correlation, along with the pressure coefficient of the  
 16 band gap, in terms of the electronic overlap between chalcogenide p-type and metal d-type orbitals. Overall, our findings identify 1T-  
 17 HfSe<sub>2</sub> as a new efficient TMD material with potential multipurpose technological applications.



## 18 ■ INTRODUCTION

19 Layered-based materials have attracted tremendous research  
 20 interest since the breakthrough of graphene.<sup>1</sup> These materials  
 21 have been widely studied owing to the intrinsic electronic  
 22 properties covering from semiconductivity to metallic behavior  
 23 along with promising catalytic performance, photolumines-  
 24 cence, and high-water resistance.<sup>2–5</sup> Particularly, layered  
 25 transition metal dichalcogenides (TMDs) exhibit unique  
 26 optical and electronic properties accompanied by a tunable  
 27 band gap.<sup>6</sup> From the structural point of view, TMDs are  
 28 defined as solids with the general stoichiometry MX<sub>2</sub> (M is a  
 29 transition metal that belongs to the groups IV, V, VI, and VII;  
 30 X = S, Se, Te) showing in-plane strong chemical bonding and  
 31 out-of-plane weak van der Waals (vdW) interactions, as  
 32 represented in Figure 1a. Based on the atomic arrangements,  
 33 TMDs are classified in three stacking polytypes denoted as 1T,  
 34 2H, and 3R that correspond to one, two, and three layers per  
 35 unit cell with a trigonal, hexagonal, and rhombohedral  
 36 structure, respectively. Note, however, that M<sub>2</sub>X<sub>3</sub> and MX  
 37 alternative stoichiometries have been recently found for  
 38 TMDs.<sup>7,8</sup> There are roughly 60 TMDs known so far, but  
 39 since MoS<sub>2</sub>, TiS<sub>2</sub>, and WS<sub>2</sub> have attracted more attention,  
 40 these three compounds are considered the workhorses among  
 41 them.<sup>9,10</sup>

42 Not surprisingly, the structural and electronic properties of  
 43 few layers and bulk TMDs can be easily tuned thanks to the  
 44 abovementioned vdW interlayer forces.<sup>11</sup> Several strategies  
 45 have been established to enhance their performance including  
 46 (i) top-down synthesis protocols moving toward low-dimen-  
 47 sional TMD counterparts,<sup>12</sup> (ii) the use of chemical dopant

agents,<sup>13</sup> (iii) the intercalation of species,<sup>14</sup> (iv) the application  
 of an electrical field,<sup>15</sup> and (v) the application of high  
 pressures.<sup>16</sup> The latter strategy brings the layers closer and thus  
 making the interlayer interactions much stronger, resulting in a  
 concomitant modulation of the TMD properties.

Recent experimental and theoretical investigations on the  
 pressure-induced properties of bulk TMDs, such as MoS<sub>2</sub>,  
 WS<sub>2</sub>, MoSe<sub>2</sub>, WSe<sub>2</sub>, and MoTe<sub>2</sub>, have reported interesting  
 semiconducting-to-metal electronic state transitions achieved  
 at  $\sim 15$ – $40$  GPa under hydrostatic conditions, depending on  
 the TMD composition.<sup>17–23</sup> The implementation of these  
 results in flexible nanoelectronic devices involves practical  
 difficulties mainly due to the high-pressure regimes required to  
 induce the metallization.<sup>24</sup> To overcome this drawback, low-  
 dimensional counterparts of TMDs coupled with uni- and  
 biaxial stress conditions have been proposed as a suitable  
 alternative to modulate the band gap at lower pressures.  
 Combined experimental and theoretical studies have success-  
 fully shown that the metallization of monolayer MoS<sub>2</sub> takes  
 place only at 3 GPa under uniaxial out-of-plane compression  
 conditions.<sup>25,26</sup>

Received: October 30, 2020

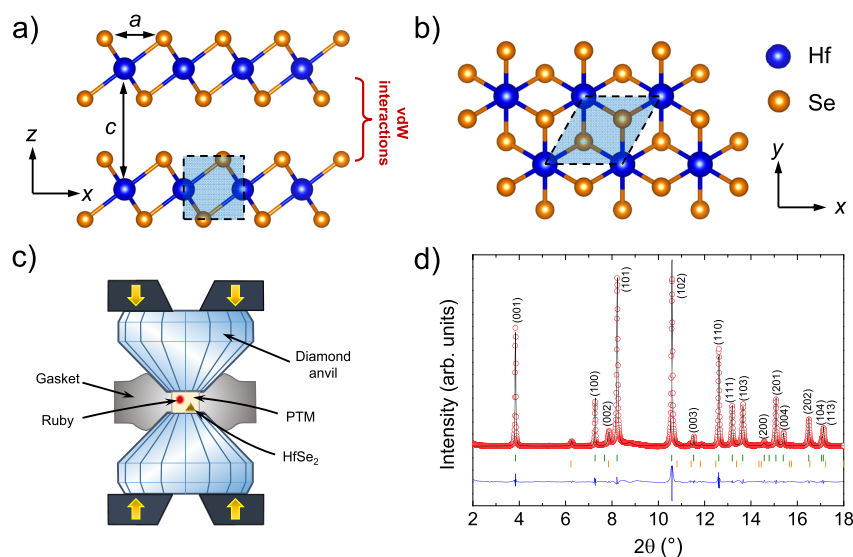


**Figure 1.** View of the crystal structure of 1T-HfSe<sub>2</sub> showing (a) the multilayered arrangement and (b) the *a-b* plane. (c) Schematic of the used high-pressure diamond anvil cell setup. (d) Observed (circles), calculated (solid line), and difference (bottom) synchrotron-XRD Rietveld profile for 1T-HfSe<sub>2</sub> at room temperature and ambient pressure. Bragg positions indicated in green correspond to 1T-HfSe<sub>2</sub>, whereas orange marks are due to a very small amount of impurity (less than 3%) identified as metallic Se.

69 All these extensive efforts have contributed significantly to  
 70 the knowledge of bulk, few layer, and monolayer TMDs under  
 71 extreme conditions. Most of the studies have been focused  
 72 only on the 2H-TMD polytype, thus demanding further  
 73 investigations over TMDs with other arrangements (e.g., 1T or  
 74 3R). In particular, 1T-TMD compounds have attracted interest  
 75 for understanding the mechanism of charge density wave order  
 76 at low temperature and its coexistence with superconductivity  
 77 under high pressure.<sup>27–29</sup> Focusing on hafnium diselenide  
 78 (1T-HfSe<sub>2</sub>), depicted in Figure 1a,b, its high carrier mobility  
 79 (above 2000 cm<sup>2</sup> V s<sup>-1</sup>), significantly larger than that of 2H-  
 80 (Mo,W)X<sub>2</sub> (~340 cm<sup>2</sup> Vs<sup>-1</sup>), is to be highlighted. Due to this  
 81 extraordinary electronic property, 1T-HfSe<sub>2</sub> emerges as one of  
 82 the most promising materials for applications in the ambit of  
 83 field-effect transistors (FETs).<sup>30,31</sup> Furthermore, the moderate  
 84 band gap of 1T-HfSe<sub>2</sub> (~1.1 eV)<sup>32</sup> opens the possibility of  
 85 using it as a high- $\kappa$  dielectric, leading to the replacement of  
 86 silicon in electronic devices.<sup>33</sup>

87 In short, the present study has the aim of providing  
 88 experimental data and theoretical interpretation on the  
 89 response of structural, vibrational, and electronic properties  
 90 of bulk 1T-HfSe<sub>2</sub> at hydrostatic high pressures. A homemade  
 91 diamond anvil cell (DAC) device has been used for performing  
 92 *in situ* high-pressure measurements, and therefore, synchrotron  
 93 X-ray diffraction, Raman spectroscopy, and optical (vis–NIR)  
 94 absorption experiments have been carried out. In addition,  
 95 density functional theory (DFT)-based calculations assist and  
 96 interpret the experiments. Our investigations demonstrate that  
 97 the 1T-HfSe<sub>2</sub> phase is highly sensitive under pressure,  
 98 reporting a metallization at ~10 GPa, which is actually the  
 99 lowest value reported to date for bulk TMDs under hydrostatic  
 100 conditions. Note that this relatively low hydrostatic pressure  
 101 may break down the technological limitations observed in  
 102 other compounds within the 2H-(Mo,W)(S, Se)<sub>2</sub> polytype  
 103 family, opening new avenues in the generation of novel flexible  
 104 nanoelectronic devices.

## EXPERIMENTAL AND COMPUTATIONAL DETAILS 105

**Samples.** HfSe<sub>2</sub> samples used in the experiments were acquired  
 106 from HQGraphene in a single crystal form. A pristine single crystal  
 107 was mechanically exfoliated and cut into smaller pieces to obtain  
 108 various samples of similar dimensions and suitable to be loaded in  
 109 the high-pressure cells. The crystal structure was checked by room-  
 110 temperature XRD, and purity and homogeneity were probed by  
 111 scanning electron microscopy (SEM) and X-ray energy-dispersive  
 112 spectroscopy (XEDS). Further details are given in Figure S1 in the  
 113 Supporting Information.

**High-Pressure Experiments.** Symmetric diamond anvil cells  
 114 (DAC) were used for high-pressure experiments. The general  
 115 operating scheme of the DAC is depicted in Figure 1c. *In situ* high-  
 116 pressure synchrotron X-ray diffraction experiments were performed at  
 117 beamline ID15B (experiment CH-5079) of the European Synchro-  
 118 tron Radiation Facility. A small piece of HfSe<sub>2</sub> was ground into fine  
 119 powder, subsequently loaded in a membrane-type DAC with 300  $\mu$ m  
 120 culet-sized diamonds. A stainless steel gasket was preindented to be  
 121 50  $\mu$ m thick, and a hole of 100  $\mu$ m in diameter was drilled. A sample  
 122 chamber was filled with helium as a pressure transmitting medium  
 123 (PTM) and two ruby chips for calibrating pressure. The beam was  
 124 operated at 0.411 Å with dimensions close to 5 × 5  $\mu$ m<sup>2</sup>. Angle-  
 125 dispersive X-ray patterns were collected with a MAR555 image plate  
 126 detector. Images were integrated by using both Fit2D and Dioptas  
 127 software. Rietveld analysis of data was performed through Fullprof  
 128 software.<sup>34,35</sup>

High-pressure Raman experiments were carried out using a  
 131 Merrill–Basset DAC device with a 400  $\mu$ m culet size. In this case,  
 132 a small single crystal flake of HfSe<sub>2</sub> was loaded into the chamber  
 133 sample of a stainless-steel gasket as well as Daphne 7373 oil as the  
 134 PTM and ruby chips as pressure markers. An XploRA PLUS confocal  
 135 Raman spectrometer equipped with excitation lines at 532 and 785 nm  
 136 and several long-distance working objectives was used to acquire the  
 137 Raman spectra.

Optical absorption under high-pressure conditions was performed  
 139 on a prototype fiber optics microscope equipped with two 25×  
 140 reflecting objectives mounted on two independent *xyz* translation  
 141 stages for a microfocus beam, the collector objective, and a third  
 142 independent *xyz* translation stage for DAC micropositioning. Optical  
 143 absorption data and images were obtained simultaneously with the  
 144 same device. Spectra in the UV–vis and NIR were recorded with an  
 145 Ocean Optics USB 2000 and NIRQUEST 512 monochromators  
 146 using Si- and InGaAs-CCD detectors, respectively. To ensure a good  
 147

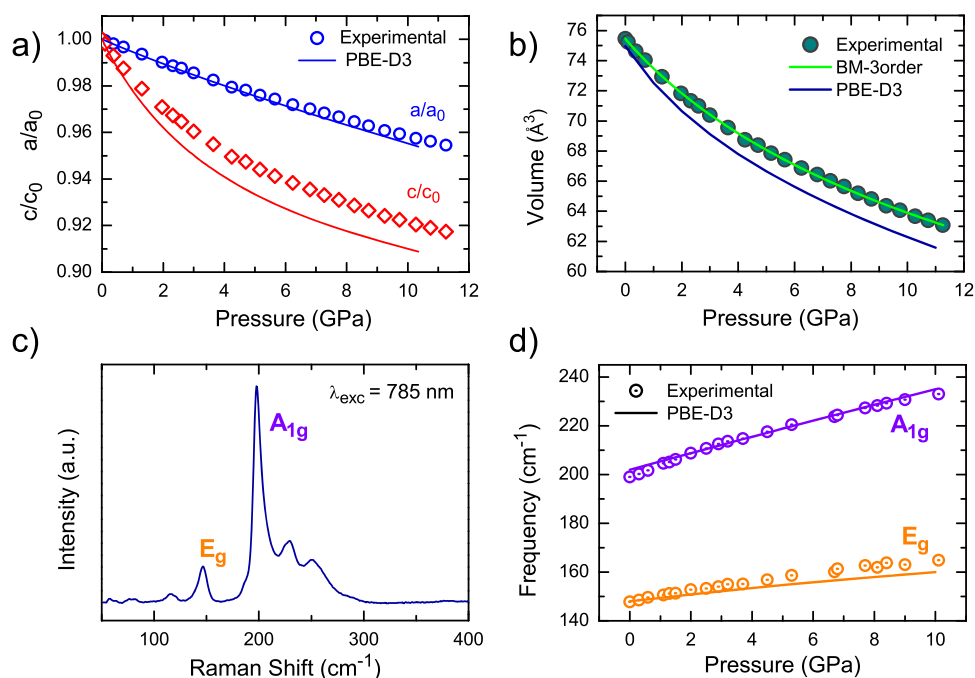


**Figure 2.** Experimental (from XRD) and theoretical pressure evolution of (a) normalized  $a/a_0$  and  $c/c_0$  lattice parameters and (b) volume of the 1T-HfSe<sub>2</sub> unit cell; third-order BM-EOS is also shown in panel (b). (c) Ambient pressure Raman spectrum of 1T-HfSe<sub>2</sub>, showing the two main vibrational modes with E<sub>g</sub> and A<sub>1g</sub> symmetry. (d) Evolution of Raman shift frequencies with pressure.

148 quality signal, the absorption spectra were obtained with an HfSe<sub>2</sub> 149 single crystal flake with a thickness of around 60 μm. Analysis of data 150 and band gap calculation methodology is detailed in Figure S2 and 151 Note S1.

152 **Density Functional Theory-Based Calculations.** First-princi- 153 ples periodic electronic structure calculations were systematically 154 performed by minimizing static total energies at selected volumes of 155 the 1T-HfSe<sub>2</sub> structure. To this end, the Vienna *ab initio* simulation 156 package (VASP)<sup>36</sup> was used by employing the Perdew–Burke– 157 Ernzerhof (PBE) implementation<sup>37</sup> within the generalized gradient 158 approximation (GGA) to the exchange–correlation (*xc*) functional. 159 Weak vdW interactions were considered by adding a semiempirical 160 dispersion potential to the conventional Kohn–Sham DFT energy 161 through a pairwise force field following Grimme’s DFT-D3 162 method.<sup>38,39</sup> This dispersion term is highly required to obtain a 163 reasonable agreement with respect to experiments even in dense 164 solids.<sup>40</sup> The Kohn–Sham equations were solved by using an 165 expansion of the valence electron density in a plane-wave basis set 166 with a kinetic energy cutoff of 500 eV. The projector-augmented wave 167 (PAW) method was included to account for the interaction between 168 the valence and the core electron densities.<sup>41,42</sup> Numerical 169 integrations in a reciprocal space were carried out by sampling  $\Gamma$ - 170 centered Monkhorst–Pack meshes,<sup>43</sup> where the numbers of 171 subdivisions along each reciprocal lattice vector  $\mathbf{b}_i$  were given by  $N_i$  172 =  $\max(1.90 |\mathbf{b}_i| + 0.5)$ . The geometry optimizations were considered 173 converged when the forces acting on the nuclei were all below  $10^{-5}$  174 eV Å<sup>-1</sup>. Note, however, that this criterion is even tight,  $10^{-8}$  eV Å<sup>-1</sup>, 175 to calculate the phonon frequencies of Raman active modes at the  $\Gamma$ - 176 point by using finite differences, as implemented in the VASP 177 package.

178 In addition, since the standard GGA calculations systematically 179 underestimate the band gap in semiconductor materials, a more 180 sophisticated approach as one based on a hybrid functional would be 181 recommended.<sup>44</sup> A state-of-the-art hybrid-based calculation strategy 182 was followed in this regard to accurately investigate the electronic 183 properties of 1T-HfSe<sub>2</sub>. Thus, the hybrid HSE06 density functional 184 was selected.<sup>45</sup> By using the hybrid HSE06 functional, 25% of the 185 short-range exchange interaction of the traditional PBE *xc* functional 186 was replaced by the short-range nonlocal Hartree–Fock exchange

187 interaction. In addition, an exchange–screening parameter  $\omega$  of 0.2 187 Å<sup>-1</sup> was applied. Particular numerical integrations by sampling  $\Gamma$ - 188 centered Monkhorst–Pack meshes with  $N_i = \max(1.30 |\mathbf{b}_i| + 0.5)$  189 were performed. 190

## 191 RESULTS AND DISCUSSION

192 **Structural Characterization.** To investigate the structure 192 of 1T-HfSe<sub>2</sub> and its evolution under hydrostatic pressure 193 conditions, *in situ* high-pressure synchrotron X-ray diffraction 194 (XRD) and Raman spectroscopy analysis coupled with DFT- 195 based calculations are carried out. The representative XRD 196 pattern for 1T-HfSe<sub>2</sub> at ambient pressure depicted in Figure 1d 197 shows a high crystallinity of the sample. The Rietveld 198 refinement confirms that 1T-HfSe<sub>2</sub> belongs to the  $P\bar{3}m1$  199 space group containing just one HfSe<sub>2</sub> formula unit per unit 200 cell with trigonal symmetry (see Table S1 for details). The cell 201 parameters are  $a = 3.7562$  Å and  $c = 6.1749$  Å. The internal 202 coordinates are (0,0,0) and (1/3,2/3,0.2560) for Hf and Se, 203 respectively. DFT-based calculations predict  $a = 3.7319$  Å,  $c =$  204  $6.2152$  Å, and  $z_{\text{Se}} = 0.2538$ , which are in good agreement with 205 the experiments. This confirms that the PBE-D3 level of 206 calculation is reasonably reliable to describe the structure of 207 1T-HfSe<sub>2</sub>. 208

209 As applied pressure increases, the XRD patterns show the 209 well-known shifting toward higher  $2\theta$  angles (see Figure S3). 210 New peaks are not observed during the compression process 211 up to 11.3 GPa, and the initial 1T-HfSe<sub>2</sub> structure is fully 212 recovered at ambient pressure. Consequently, the compression/ 213 decompression cycle is completely reversible (see Figure 214 S3 and Note S2). This outstanding mechanical stability is one 215 of the main desired requirements for the development of future 216 electronic devices operating under harsh conditions. 217

218 At this respect, we would like to notice that a pressure- 218 induced phase transition to a C2/m monoclinic structure was 219 recently reported in 1T-TiTe<sub>2</sub> showing coexistence with the 220 trigonal phase in a wide range of pressures from ~5 to 19 221



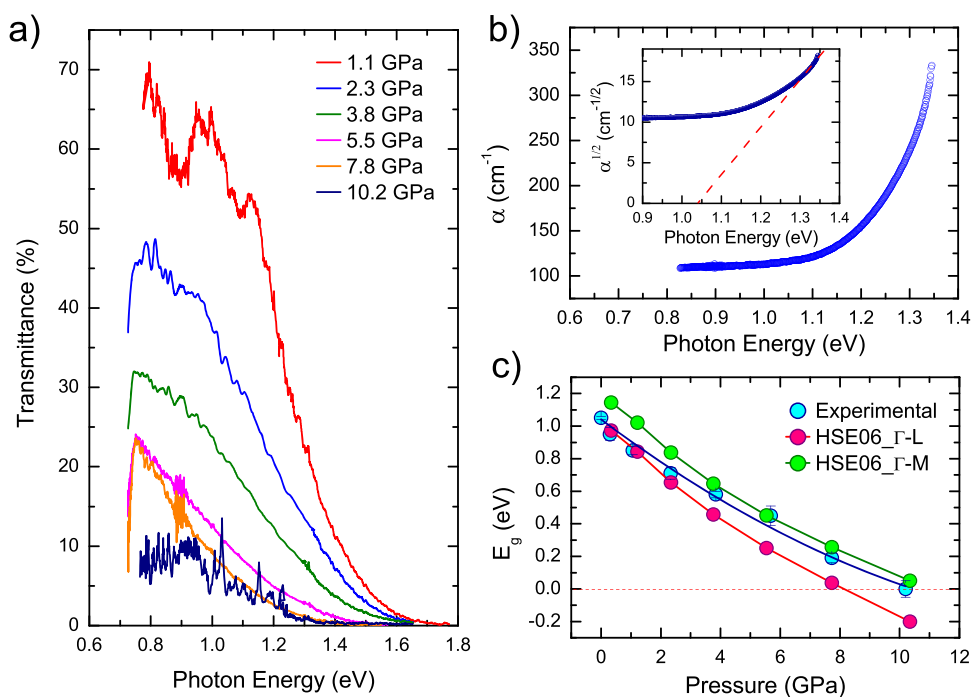


**Figure 3.** (a) Pressure evolution of the vis–NIR transmittance spectra for 1T–HfSe<sub>2</sub>. (b) Optical absorption coefficient versus photon energy at ambient pressure (the inset shows the linear extrapolation to estimate the band gap). (c) Evolution of the experimental and theoretical calculations of the band gap energy with pressure.

222 GPa.<sup>46–48</sup> The claimed generality of this transformation in  
 223 TMD MX<sub>2</sub> compounds was later examined by Mora-Fonz *et*  
 224 *al.*<sup>49</sup> The emergence of the monoclinic C2/m structure is  
 225 explicitly ruled out in their exhaustive computational study of  
 226 the 1T–TiSe<sub>2</sub> polytype. They found that this trigonal structure  
 227 is the stable phase up to 25 GPa and conclude that the  
 228 pressure-induced polymorphic sequence is still an open  
 229 question. For 1T–TiS<sub>2</sub>, instead of the C2/m monoclinic  
 230 structure, a cotunnite-like polymorph is proposed as the high-  
 231 pressure structure where the trigonal polytype transits at 16.2  
 232 GPa.<sup>50</sup> The lower oxidation power of Te and the distinctive  
 233 role of the 5p orbital in Te-based TMDs, compared to S and  
 234 Se counterparts, should be taken into account to explain the  
 235 rich polymorphism of the TMD family according to the high-  
 236 pressure study of Léger *et al.* in 1T–IrTe<sub>2</sub>.<sup>51</sup> This is of relevance  
 237 to our work showing that, in all these experimental and  
 238 theoretical studies, the trigonal 1T polytype is always observed  
 239 in the pressure range where our experiments and calculations  
 240 have been performed.

241 The experimental and computed pressure dependence of the  
 242 unit cell volume  $V$  and lattice parameters  $a$  and  $c$  are shown in  
 243 Figure 2a and Figure 2b, respectively.  $V$ ,  $a$ , and  $c$  exhibit  
 244 smooth variations as pressure increases for both experiments  
 245 and theory. Computational results are in reasonable agreement  
 246 with the experiments, although at high pressure, the calculated  
 247 lattice parameter reduction along the interlayer  $c$ -axis direction  
 248 is predicted to be slightly higher than the experimental one.  
 249 This deviation from the experiments can be attributed to the  
 250 description of the vdW interactions that is reasonable in the  
 251 absence of pressure but is progressively underestimated as  
 252 pressure increases according to the D3 correction. Overall, the  
 253 calculated trends observed under pressure are well-described  
 254 compared to experiments.

255 Quantitatively speaking, the pressure evolution of  $a$ ,  $c$ , and  $V$   
 256 is carried out by fitting analytical functions to the data. The

experimental third-order Birch–Murnaghan (BM3) equation  
 of state (EOS)<sup>52,53</sup> (see Figure 2b) provides a zero-pressure  
 volume ( $V_0$ ) equal to 75.42 Å<sup>3</sup> and an isothermal zero pressure  
 bulk modulus ( $B_0$ ) along with its first pressure derivative ( $B_0'$ )  
 of 34.5 GPa and 6.9, respectively. DFT calculations lead to  $V_0$   
 = 74.96 Å<sup>3</sup>,  $B_0$  = 29.2 GPa, and  $B_0'$  = 7.0, in reasonable  
 agreement with the experimental results. Here, it must be  
 noted that the low  $B_0$  value compared with other compounds  
 within the MX<sub>2</sub> crystal family (for example, 57 and 62 GPa for  
 MoS<sub>2</sub> and MoSe<sub>2</sub>, respectively)<sup>17,19</sup> shows an interesting result  
 that might anticipate a low metallization pressure for 1T–HfSe<sub>2</sub>,  
 assuming that the metallization is a consequence of short-  
 distance interlayer interactions.

Concerning the effect of pressure on the unit cell  
 parameters, it is more pronounced in the  $c$  axis than in the  $a$   
 axis. The former is reduced around 8.3%, whereas the latter is  
 only reduced around half of it, ~4.5%, at the maximum  
 reached pressure in our experiments, close to 11 GPa. Linear  
 isothermal compressibility ( $k_i$ ) values of  $k_a$  = 5.51 TPa<sup>-1</sup> and  $k_c$   
 = 21.0 TPa<sup>-1</sup> and  $k_a$  = 5.51 TPa<sup>-1</sup> and  $k_c$  = 29.6 TPa<sup>-1</sup> are  
 obtained from the experimental and calculated data,  
 respectively. These values are fully consistent with the trends  
 displayed in Figure 2a and evidence a clear pressure-induced  
 structural anisotropy in 1T–HfSe<sub>2</sub>. Likewise, the pressure  
 evolution of Se–Se and Hf–Se interatomic distances  
 corroborates this observation since the reduction of the Se–  
 Se interlayer distance is much more pronounced than  
 corresponding to the intralayer Hf–Se one (see Figure S4).  
 All these structural results have obvious implications in the  
 electronic behavior of this polytype as we will discuss later.

Following with the structural characterization, Raman  
 spectroscopy has been broadly used to characterize TMD-  
 derived materials.<sup>54,55</sup> The Raman spectrum of 1T–HfSe<sub>2</sub>  
 clearly shows two signals centered at 147 and 199  
 cm<sup>-1</sup> corresponding to normal modes of E<sub>g</sub> and A<sub>1g</sub>

292 symmetry in good agreement with previous works, respec-  
 293 tively.<sup>56,57</sup> The  $E_g$  mode corresponds to in-plane vibrations,  
 294 whereas the  $A_{1g}$  one is associated with out-of-plane atomic  
 295 movements. Interestingly, the DFT-based calculations give  
 296 frequencies at 148 and 202  $\text{cm}^{-1}$ , respectively. Note that the  
 297 computed Raman frequency modes match quite well in the  
 298 absence of pressure. Not surprisingly, both Raman modes shift  
 299 toward high frequencies at increasing pressure (Figure 2d).  
 300 The experimental pressure coefficients for  $E_g$  and  $A_{1g}$  modes  
 301 are 1.67 and 3.33  $\text{cm}^{-1} \text{GPa}^{-1}$ , respectively. Again, our  
 302 calculations reproduce reasonably well these values. The weak  
 303 interactions along the  $c$ -axis direction are significantly sensitive  
 304 to pressure effects. This structural argument directly explains  
 305 why the  $A_{1g}$  pressure coefficient is higher compared to that of  
 306 the  $E_g$  mode. The different response of the vibrational modes,  
 307 depending on whether they are in-plane or out-of-plane, is  
 308 another manifestation of pressure-induced anisotropy exhibited  
 309 by this material (see Figure S5 for a detailed scheme of normal  
 310 modes and the Raman spectra under pressure).

311 **Electronic Characterization.** We show now results from  
 312 the analysis of the electronic properties of 1T-HfSe<sub>2</sub> and, more  
 313 interestingly, their evolution under pressure. To this end, *in*  
 314 *situ* high-pressure optical absorption experiments coupled with  
 315 DFT-based electron band calculations are carried out. The  
 316 vis–NIR absorption spectra are analyzed in detail (Figure 3a).  
 317 First, we focus on the spectrum in the absence of pressure.  
 318 Plotting the optical absorption coefficient square root versus  
 319 photon energy allows one to estimate the band gap,  $E_g$ , using a  
 320 linear extrapolation (see details in Figure S2 and Note S1). In  
 321 the absence of pressure, 1T-HfSe<sub>2</sub> yields to an indirect gap of  
 322 1.05 eV estimated by the linear extrapolation (Figure 3b,  
 323 inset). Our experiments at zero pressure are in good agreement  
 324 with previous studies.<sup>33,58,59</sup> In addition, accurate DFT-based  
 325 calculations using the hybrid HSE06  $xc$  functional reveal two  
 326 close indirect gaps at  $\Gamma$ –L (0.97 eV) and  $\Gamma$ –M (1.14 eV), as  
 327 shown in the band structure depicted in Figure 4a. This leads  
 328 to a theoretical  $E_g$  value of 0.97 eV, in close agreement with the  
 329 experimental one.

330 The effect of pressure is analyzed based on the vis–NIR  
 331 spectra depicted in Figure 3a. A significant reduction of the  
 332 transmittance within the transmission window below 1.2 eV is  
 333 observed as pressure increases. Interestingly, the transmission  
 334 edge becomes almost negligible at 10.2 GPa. This result  
 335 confirms the closure of the band gap and evidences the  
 336 metallization of 1T-HfSe<sub>2</sub>. The linear extrapolation method  
 337 (see the inset in Figure 3b) has been also used to evaluate the  
 338 pressure evolution of the band gap. Pressure evolution of the  
 339 band gap energy is shown in Figure 3c. The  $E_g$  narrowing  
 340 progresses steadily and smoothly as the pressure increases. A  
 341 reduction of 50% in the band gap is already achieved at 4 GPa.  
 342 The  $E_g$  pressure evolution exhibits an almost linear trend, easily  
 343 represented with a second-order polynomial, similar to other  
 344 well-known TMDs such as MoS<sub>2</sub> and MoSe<sub>2</sub>.<sup>17,19</sup>

345 Further interesting results are found in the analysis of the  
 346 abovementioned calculated indirect gaps at  $\Gamma$ –L and  $\Gamma$ –M  
 347 regions of the Brillouin zone. The former shows the smallest  
 348 band gap along the investigated pressure range and disappears  
 349 at 8.1 GPa, whereas the latter is zero at around 10.9 GPa by an  
 350 extrapolation analysis (Figure 3c). These computational results  
 351 pinpoint the emergence of a metal state observed in the  
 352 experiments and confirm that bulk 1T-HfSe<sub>2</sub> becomes metallic  
 353 at  $\sim$ 10 GPa, the lowest metallization pressure known so far in  
 354 MX<sub>2</sub> TMD materials (see Figure 4b).

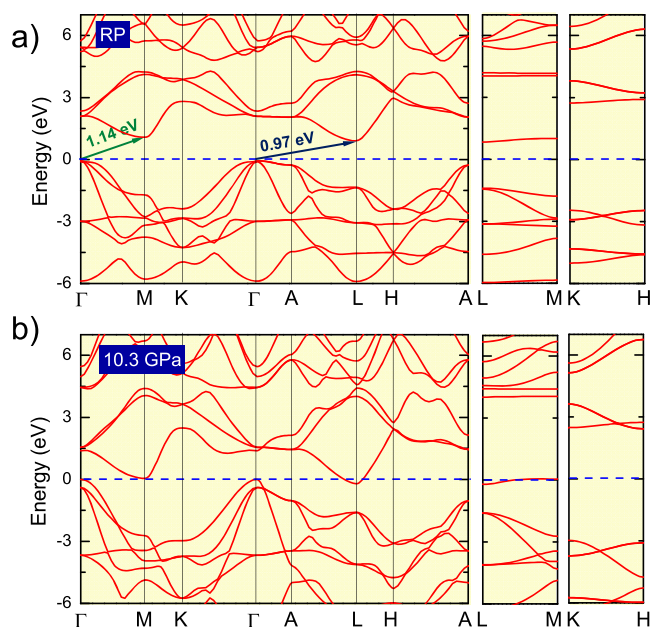
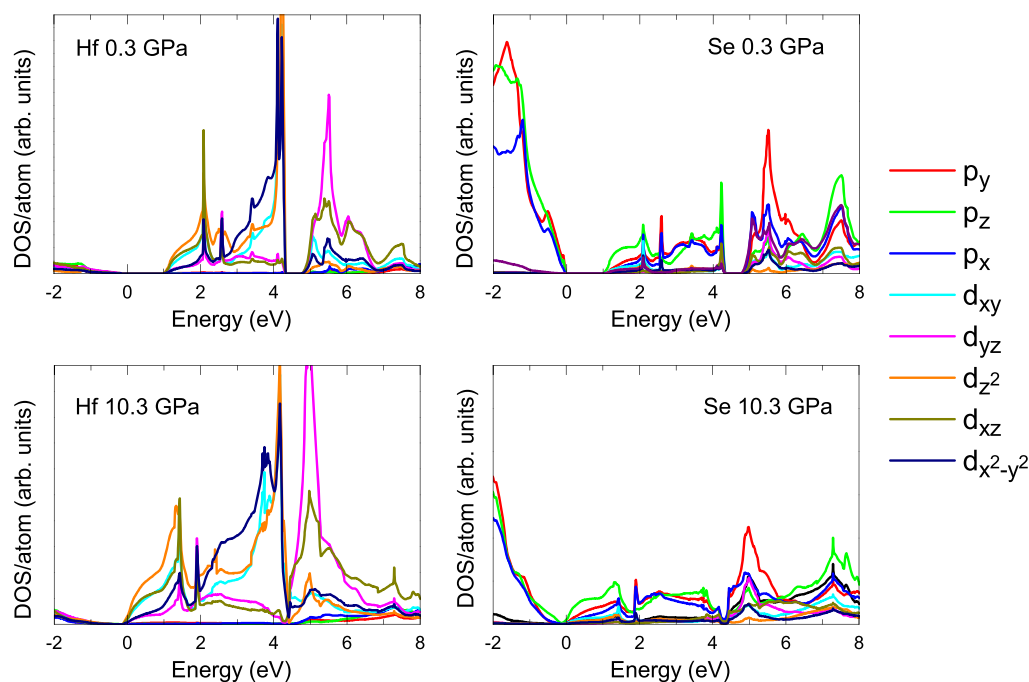


Figure 4. DFT-based calculations of the band structures on 1T-HfSe<sub>2</sub> at (a) ambient pressure and (b) metallization pressure. Red lines indicate the Fermi level, and arrows show the indirect band gaps.

To identify the atomic orbitals involved in the metallization  
 of 1T-HfSe<sub>2</sub>, the partial density of states (DOS) depicted in  
 Figure 5 is discussed. This analysis reveals a predominant  
 contribution of the Se 4p orbitals in the valence band (VB),  
 whereas the Hf 5d orbitals are the ones dominating the  
 conduction band (CB). When 1T-HfSe<sub>2</sub> is subjected to high  
 pressure, the contribution from the Se  $p_z$  in the VB and those  
 of the metal  $d_{z^2}$ ,  $d_{xz}$ , and  $d_{yz}$  orbitals in the CB become more  
 important, therefore decreasing the participation of the  $p_x$  and  
 $p_y$  orbitals of the chalcogen and  $d_{xy}$  and  $d_{x^2-y^2}$  of Hf.

This means that the orbitals with electron density localized  
 along the  $z$  direction increase their contribution in the density  
 of states of the VB and CB by the effect of pressure. This trend  
 is directly connected with the structural anisotropy of this  
 material, as described in the previous structural character-  
 ization. From the chemical point of view, the hydrostatic  
 pressure induces an effective overlapping between the orbitals  
 directed along the  $z$  direction, and then, noncovalent  
 interactions are strengthened.<sup>26</sup> As a consequence, we  
 conclude that the CB is stabilized thanks to the effective  
 overlapping of these orbitals, producing the vanishing of the  
 band gap and the eventual metallization of 1T-HfSe<sub>2</sub> under  
 pressure.

All these results point out that the metallization of 1T-HfSe<sub>2</sub>  
 is conditioned mainly by its response to hydrostatic pressure  
 and particularly by the compressibility along the  $c$  axis. An  
 interesting comparison is schemed in Figure 6a, where the  $B_0$   
 parameter of different TMDs is included along with our result  
 corresponding to 1T-HfSe<sub>2</sub>. The latter presents the lowest  
 $B_0$  values among the selected TMD family. It is probably due to a  
 good compromise between the efficient overlapping of the  
 chalcogen's  $p$  orbitals, which are much more effective in  
 selenides than in sulfides, and the large Hf ionic radius in  
 comparison with other metals as Mo or W. Both factors favor a  
 strengthening of noncovalent interactions along the  $z$   
 direction, which justifies a higher compressibility and less  
 rigidity of this material. In fact, such a behavior has previously



**Figure 5.** Partial density of states (DOS) for Hf (left) and Se (right) atoms at 0.3 GPa (upper) and at metallization pressure (lower).

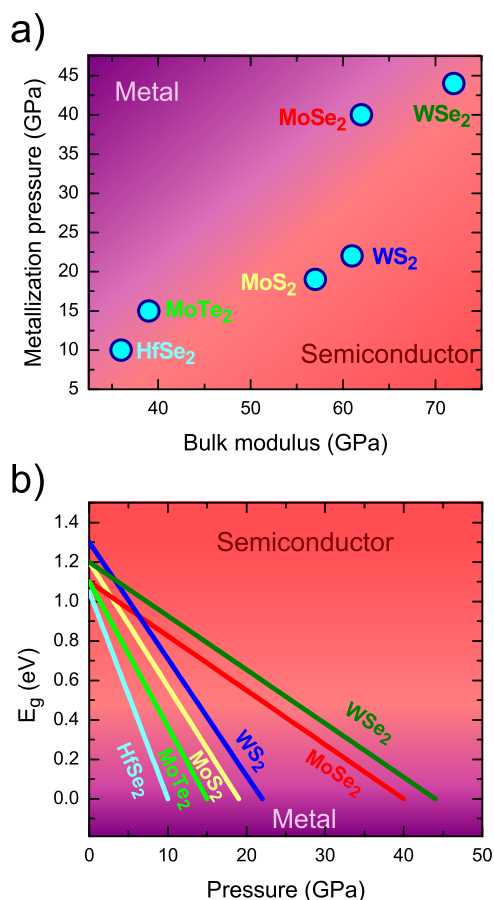


**Figure 6.** (a) Metallization pressure versus bulk modulus for different TMDs. (b) Evolution of the band gap energy with pressure for different TMDs, showing the metallization pressure for each material.

These results reveal a correlation between the bulk modulus and the metallization pressure for different TMDs explored in Figure 6a. It is clearly seen that the more compressible is a material, the lower its metallization pressure is expected, and thus, 1T-HfSe<sub>2</sub> has been positioned in a very attractive pressure regime, close to 10 GPa. 2H-MoTe<sub>2</sub>, 2H-MoS<sub>2</sub>, 2H-MoW<sub>2</sub>, 2H-MoSe<sub>2</sub>, and 2H-WSe<sub>2</sub> follow, in this order, increasing values of both  $B_0$  and  $P_{\text{met}}$ . Analogously, the band gap versus pressure plotted in Figure 6b show that the linear trends (guide to the eye) of 2H-MX<sub>2</sub> (M = Mo, W; X = S, Se, Te)<sup>17–20,22,23</sup> and 1T-HfSe<sub>2</sub> (this work) also follow the same sequence. Clearly, the reduction of  $E_g$  in 1T-HfSe<sub>2</sub> occurs at the highest pressure rate, close to 0.1 eV·GPa<sup>-1</sup>. We thus conclude that 1T-HfSe<sub>2</sub> presents attractive tunable electronic properties that can be easily modulated by the application of relatively moderate pressures.

## CONCLUSIONS

We have undertaken a complete and detailed study on bulk 1T-HfSe<sub>2</sub>, covering the analysis of its structural, dynamical, and electronic properties up to 12 GPa. We have combined experiments and theoretical calculations to shed light on this TMD material to understand its behavior under pressure. Our results conclude that 1T-HfSe<sub>2</sub> shows a highly sensitive response to pressure application, giving increase to a pressure-driven metallization at around 10 GPa, which is actually the lowest value found to date among common bulk TMD-derived materials. The theoretical calculations are in good agreement with the experimental observations, and the correlation between electronic behavior of the solid and the mechanical response of its crystallographic structure under pressure has been evidenced. Within the studied pressure range, there is no first-order structural transition found, and both structure and electronic behavior are completely reversible, which is an essential requirement for the development of future electronic devices operating under harsh conditions. This scenario situates 1T-HfSe<sub>2</sub> in a privileged

392 been theoretically predicted by Guzmán and Strachan for  
393 TMDs.<sup>60</sup>



430 position compared to other TMDs. In fact, most usual  
431 strategies for effectively tuning the electronic properties of  
432 these systems concern the dimensionality reduction, working  
433 at the nanoscale (monolayers). Through the application of  
434 hydrostatic pressure, some materials require even more than 60  
435 GPa for inducing a semiconductor–metal electronic transition.  
436 In contrast, 1T-HfSe<sub>2</sub> would allow us to work within the  
437 macroscopic scale, being able to significantly modulate their  
438 optoelectronic properties by means of moderate pressure  
439 application.

## 440 ■ ASSOCIATED CONTENT

### 441 ■ Supporting Information

442 The Supporting Information is available free of charge at  
443 <https://pubs.acs.org/doi/10.1021/acs.inorgchem.0c03223>.

444 Additional supporting figures, tables, and notes showing  
445 SEM, XEDS, optical density explorations, XRD patterns,  
446 pressure evolution, crystallographic data, and other  
447 experiments (PDF)

## 448 ■ AUTHOR INFORMATION

### 449 Corresponding Author

450 Adrián Andrada-Chacón – MALTA-Consolider Team,  
451 Departamento de Química Física, Facultad de Ciencias  
452 Químicas, Universidad Complutense de Madrid, Madrid  
453 28040, Spain; [orcid.org/0000-0003-4504-3197](https://orcid.org/0000-0003-4504-3197);  
454 Email: [a.andrada@ucm.es](mailto:a.andrada@ucm.es)

### 455 Authors

456 Ángel Morales-García – Departament de Ciència de Materials  
457 i Química Física & Institut de Química Teòrica i  
458 Computacional (IQTCUB), Universitat de Barcelona,  
459 Barcelona 08028, Spain; [orcid.org/0000-0003-0491-1234](https://orcid.org/0000-0003-0491-1234)

461 Miguel A. Salvadó – MALTA-Consolider Team,  
462 Departamento de Química Física y Analítica, Universidad de  
463 Oviedo, Oviedo 33006, Spain

464 Pilar Perterra – MALTA-Consolider Team, Departamento de  
465 Química Física y Analítica, Universidad de Oviedo, Oviedo  
466 33006, Spain

467 Ruth Franco – MALTA-Consolider Team, Departamento de  
468 Química Física y Analítica, Universidad de Oviedo, Oviedo  
469 33006, Spain

470 Gastón Garbarino – European Synchrotron Radiation  
471 Facility, Grenoble 38043, France

472 Mercedes Taravillo – MALTA-Consolider Team,  
473 Departamento de Química Física, Facultad de Ciencias  
474 Químicas, Universidad Complutense de Madrid, Madrid  
475 28040, Spain

476 José A. Barreda-Argüeso – MALTA-Consolider Team,  
477 CITIMAC, Universidad de Cantabria, Santander 39005,  
478 Spain

479 Jesús González – MALTA-Consolider Team, CITIMAC,  
480 Universidad de Cantabria, Santander 39005, Spain

481 Valentín G. Baonza – MALTA-Consolider Team,  
482 Departamento de Química Física, Facultad de Ciencias  
483 Químicas, Universidad Complutense de Madrid, Madrid  
484 28040, Spain

485 Jose Manuel Recio – MALTA-Consolider Team,  
486 Departamento de Química Física y Analítica, Universidad de  
487 Oviedo, Oviedo 33006, Spain; [orcid.org/0000-0002-3182-7508](https://orcid.org/0000-0002-3182-7508)

Javier Sánchez-Benítez – MALTA-Consolider Team, 489  
Departamento de Química Física, Facultad de Ciencias 490  
Químicas, Universidad Complutense de Madrid, Madrid 491  
28040, Spain; [orcid.org/0000-0002-3108-6594](https://orcid.org/0000-0002-3108-6594) 492

Complete contact information is available at: 493  
<https://pubs.acs.org/doi/10.1021/acs.inorgchem.0c03223> 494

### 495 Author Contributions

A.A.-C. and J.S.-B. conceived the idea and led the project. A.A.- 496  
C. designed the experiments and performed the synchrotron 497  
XRD, Raman, and optical absorption measurements. A.M.-G., 498  
M.A.S., P.P., R.F., and J.M.R. conducted the theoretical 499  
calculations. G.G. contributed to the synchrotron XRD 500  
measurements at high pressure. J.A.B.-A. and J.G. contributed 501  
to the optical absorption experiments at high pressure and 502  
analysis of data. M.T. and V.G.B. contributed to the analysis, 503  
interpretation, and discussion of results. A.A.-C., A.M.-G., 504  
J.M.R., and J.S.-B. wrote the manuscript with the help of all the 505  
authors. All the authors commented on the final manuscript. 506  
J.S.-B. supervised the project. 507

### 508 Notes

The authors declare no competing financial interest. 509

## 510 ■ ACKNOWLEDGMENTS

We are grateful to the Ministerio de Ciencia e Innovación 511  
(projects PGC2018-094814-B-C21 and PGC2018-094814-B- 512  
C22), the Principado de Asturias-FICYT (FC-GRUPIN-IDI/ 513  
2018/000177), and FEDER (RED2018-102612-T) for the 514  
financial support. We are grateful to ESRF for making all 515  
facilities available. A.M.-G. thanks the Spanish MICIUN for a 516  
Juan de la Cierva postdoctoral contract (IJCI-2017-31979) and 517  
María de Maeztu MDM-2017-0767 grant. 518

## 519 ■ REFERENCES

- (1) Geim, A. K.; Novoselov, K. S. The Rise of Graphene. *Nat. Mater.* 2007, 6, 183–191. 520
- (2) Butler, S. Z.; Hollen, S. M.; Cao, L.; Cui, Y.; Gupta, J. A.; 521  
Gutiérrez, H. R.; Heinz, T. F.; Hong, S. S.; Huang, J.; Ismach, A. F.; 522  
Johnson-Halperin, E.; Kuno, M.; Plashnitsa, V. V.; Robinson, R. D.; 523  
Ruoff, R. S.; Salahuddin, S.; Shan, J.; Shi, L.; Spencer, M. G.; 524  
Terrones, M.; Windl, W.; Goldberger, J. E. Progress, Challenges, and 525  
Opportunities in Two-Dimensional Materials Beyond Graphene. *ACS* 526  
*Nano* 2013, 7, 2898–2926. 527
- (3) Liu, Y.; Weiss, N. O.; Duan, X.; Cheng, H.-C.; Huang, Y.; Duan, 528  
X. Van der Waals Heterostructures and Devices. *Nat. Rev. Mater.* 529  
2016, 1, 16042. 530
- (4) Centi, G.; Perathoner, S. Catalysis by Layered Materials: A 531  
Review. *Microporous Mesoporous Mater.* 2008, 107, 3–15. 532
- (5) Purdie, D. G.; Pugno, N. M.; Taniguchi, T.; Watanabe, K.; 533  
Ferrari, A. C.; Lombardo, A. Cleaning Interfaces in Layered Materials 534  
Heterostructures. *Nat. Commun.* 2018, 9, 5387. 535
- (6) Choi, W.; Choudhary, N.; Han, G. H.; Park, J.; Akinwande, D.; 536  
Lee, Y. H. Recent Development of Two-Dimensional Transition 537  
Metal Dichalcogenides and Their Applications. *Mater. Today* 2017, 538  
20, 116–130. 539
- (7) Zhang, J.; Peng, Z.; Soni, A.; Zhao, Y.; Xiong, Y.; Peng, B.; 540  
Wang, J.; Dresselhaus, M. S.; Xiong, Q. Raman Spectroscopy of Few- 541  
Quintuple Layer Topological Insulator Bi<sub>2</sub>Se<sub>3</sub> Nanoplatelets. *Nano* 542  
*Letts.* 2011, 11, 2407–2414. 543
- (8) Zhou, X.; Cheng, J.; Zhou, Y.; Cao, T.; Hong, H.; Liao, Z.; Wu, 544  
S.; Peng, H.; Liu, K.; Yu, D. Strong Second-Harmonic Generation in 545  
Atomic Layered GaSe. *J. Am. Chem. Soc.* 2015, 137, 7994–7997. 546
- (9) Manzeli, S.; Ovchinnikov, D.; Pasquier, D.; Yazvey, O. V.; Kis, A. 547  
2D Transition Metal Dichalcogenides. *Nat. Rev. Mater.* 2017, 2, 548  
17033. 549  
550

- (10) Chhowalla, M.; Shin, H. S.; Eda, G.; Li, L.-J.; Loh, K.-P.; Zhang, H. The Chemistry of Two-Dimensional Layered Transition Metal Dichalcogenide Nanosheets. *Nat. Chem.* **2013**, *5*, 263–275.
- (11) Qiu, X.; Ji, W. Illuminating Interlayer Interactions. *Nat. Mater.* **2018**, *17*, 211–213.
- (12) Lv, R.; Robinson, J. A.; Schaak, R. E.; Sun, D.; Sun, Y.; Mallouk, T. E.; Terrones, M. Transition Metal Dichalcogenides and Beyond: Synthesis, Properties, and Applications of Single- and Few-Layer Nanosheets. *Acc. Chem. Res.* **2015**, *48*, 56–64.
- (13) Balasubramaniam, B.; Singh, N.; Kar, P.; Tyagi, A.; Prakash, J.; Gupta, R. K. Engineering of Transition Metal Dichalcogenide-Based 2D Nanomaterials Through Doping for Environmental Applications. *Mol. Syst. Des. Eng.* **2019**, *4*, 804–827.
- (14) Jung, Y.; Zhou, Y.; Cha, J. J. Intercalation in Two-Dimensional Transition Metal Chalcogenides. *Inorg. Chem. Front.* **2016**, *3*, 452–463.
- (15) Liu, F.; Zhou, J.; Zhu, C.; Liu, Z. Electric Field Effect in Two-Dimensional Transition Metal Dichalcogenides. *Adv. Funct. Mater.* **2017**, *27*, 1602404.
- (16) Mao, H.-K.; Chen, B.; Chen, J.; Li, K.; Lin, J.-F.; Yang, W.; Zheng, H. Recent Advances in High-Pressure Science and Technology. *Matter Radiat. Extremes* **2016**, *1*, 59–75.
- (17) Nayak, A. P.; Bhattacharyya, S.; Zhu, J.; Liu, J.; Wu, X.; Pandey, T.; Jin, C.; Singh, A. K.; Akinwande, D.; Lin, J.-F. Pressure-Induced Semiconducting to Metallic Transition in Multilayered Molybdenum Disulfide. *Nat. Commun.* **2014**, *5*, 3731.
- (18) Nayak, A. P.; Yuan, Z.; Cao, B.; Liu, J.; Wu, J.; Moran, S. T.; Li, T.; Akinwande, D.; Jin, C.; Lin, J.-F. Pressure-Modulated Conductivity, Carrier Density, and Mobility of Multilayered Tungsten Disulfide. *ACS Nano* **2015**, *9*, 9117–9123.
- (19) Zhao, Z.; Zhang, H.; Yuan, H.; Wang, S.; Lin, Y.; Zeng, Q.; Xu, G.; Liu, Z.; Solanki, G. K.; Patel, K. D.; Cui, Y.; Hwang, H. Y.; Mao, W. L. Pressure Induced Metallization with Absence of Structural Transition in Layered Molybdenum Diselenide. *Nat. Commun.* **2015**, *6*, 7312.
- (20) Liu, B.; Han, Y.; Gao, C.; Ma, Y.; Peng, G.; Wu, B.; Liu, C.; Wang, Y.; Hu, T.; Cui, X.; Ren, W.; Li, Y.; Su, N.; Liu, H.; Zou, G. Pressure Induced Semiconductor-Semimetal Transition in WSe<sub>2</sub>. *J. Phys. Chem. C* **2010**, *114*, 14251–14254.
- (21) Wang, X.; Chen, X.; Zhou, Y.; Park, C.; An, C.; Zhou, Y.; Zhang, R.; Gu, C.; Yang, W.; Yang, Z. Pressure-Induced Iso-Structural Phase Transition and Metallization in WSe<sub>2</sub>. *Sci. Rep.* **2017**, *7*, 46694.
- (22) Qi, Y.; Naumov, P. G.; Ali, M. N.; Rajamathi, C. R.; Schnelle, W.; Barkalov, O.; Hanfland, M.; Wu, S.-C.; Shekhar, C.; Sun, Y.; Süß, V.; Schmidt, M.; Schwarz, U.; Pippel, E.; Werner, P.; Hillebrand, R.; Förster, T.; Kampert, E.; Parkin, S.; Cava, R. J.; Felser, C.; Yan, B.; Medvedev, S. A. Superconductivity in Weyl Semimetal Candidate MoTe<sub>2</sub>. *Nat. Commun.* **2016**, *7*, 11038.
- (23) Zhao, X.-M.; Liu, H.-Y.; Goncharov, A. F.; Zhao, Z.-W.; Struzhkin, V. V.; Mao, H.-K.; Gavriluk, A. G.; Chen, X.-J. Pressure Effect on the Electronic, Structural, and Vibrational Properties of Layered 2H-MoTe<sub>2</sub>. *Phys. Rev. B* **2019**, *99*, No. 024111.
- (24) Akinwande, D.; Petrone, N.; Hone, J. Two-Dimensional Flexible Nanoelectronics. *Nat. Commun.* **2014**, *5*, 5678.
- (25) Peña-Álvarez, M.; del Corro, E.; Morales-García, A.; Kavan, L.; Kalbac, M.; Frank, O. Single Layer Molybdenum Disulfide Under Direct Out-of-Plane Compression: Low-Stress Band-Gap Engineering. *Nano Lett.* **2015**, *15*, 3139–3146.
- (26) García, A. M.; del Corro, E.; Kalbac, M.; Frank, O. Tuning the Electronic Properties of Monolayer and Bilayer Transition Metal Dichalcogenide Compounds under Direct Out-of-Plane Compression. *Phys. Chem. Chem. Phys.* **2017**, *19*, 13333–13340.
- (27) Ritschel, T.; Trinckauf, J.; Garbarino, G.; Hanfland, M.; Zimmermann, M. V.; Berger, H.; Büchner, B.; Geck, J. Pressure Dependence of the Charge Density Wave in 1T-TaS<sub>2</sub> and its Relation to Superconductivity. *Phys. Rev. B* **2013**, *87*, 125135.
- (28) Dutta, U.; Malavi, P. S.; Sahoo, S.; Joseph, B.; Karmakar, S. Pressure-Induced Superconductivity in Semimetallic 1T-TiTe<sub>2</sub> and Its Persistence Upon Decompression. *Phys. Rev. B* **2018**, *97*, 060503.
- (29) Sahoo, S.; Dutta, U.; Harnagea, L.; Sood, A. K.; Karmakar, S. Pressure-Induced Suppression of Charge Density Wave and Emergence of Superconductivity in 1T-VSe<sub>2</sub>. *Phys. Rev. B* **2020**, *101*, No. 014514.
- (30) Kang, M.; Rathi, S.; Lee, I.; Lim, D.; Wang, J.; Kahn, M. A.; Kim, G.-H. Electrical Characterization of Multilayer HfSe<sub>2</sub> Field-Effect Transistors on SiO<sub>2</sub> Substrates. *Appl. Phys. Lett.* **2015**, *97*, 143108.
- (31) Yin, L.; Xu, K.; Wen, Y.; Wang, Z.; Huang, Y.; Wang, F.; Shifa, T. A.; Cheng, R.; Ma, H.; He, J. Ultrafast and Ultrasensitive Phototransistors Based on Few-Layered HfSe<sub>2</sub>. *Appl. Phys. Lett.* **2016**, *109*, 213105.
- (32) Yue, R.; Barton, A. T.; Zhu, H.; Azcatl, A.; Pena, L. F.; Wang, J.; Peng, X.; Lu, N.; Cheng, X.; Addou, R.; McDonnell, S.; Colombo, L.; Hsu, J. W. P.; Kim, J.; Kim, M. J.; Wallace, R. M.; Hinkle, C. L. HfSe<sub>2</sub> Thin Films: 2D Transition Metal Dichalcogenides Grown by Molecular Beam Epitaxy. *ACS Nano* **2015**, *9*, 474–480.
- (33) Mleczo, M. J.; Zhang, C.; Lee, H. R.; Kuo, H.-H.; Magyariköpe, B.; Moore, R. G.; Shen, Z.-X.; Fisher, I. R.; Nishi, Y.; Pop, E. HfSe<sub>2</sub> and ZrSe<sub>2</sub>: Two-Dimensional Semiconductors with Native High-κ Oxides. *Sci. Adv.* **2017**, *3*, No. e1700481.
- (34) Prescher, C.; Prakapenka, V. B. DIOPTAS: a Program for Reduction of Two-dimensional X-ray Diffraction Data and Data Exploration. *High Press. Res.* **2015**, *35*, 223–230.
- (35) Rodríguez-Carvajal, J. Recent Advances in Magnetic Structure Determination by Neutron Powder Diffraction. *Physica B: Condens. Matter* **1993**, *192*, 55–69.
- (36) Kresse, G.; Furthmüller, J. Efficient Iterative Schemes for ab initio Total-Energy Calculations Using a Plane-Wave Basis Set. *Phys. Rev. B* **1996**, *54*, 11169–11186.
- (37) Perdew, J. P.; Burke, K.; Ernzerhof, M. Generalized Gradient Approximation Made Simple. *Phys. Rev. Lett.* **1996**, *77*, 3865–3868.
- (38) Grimme, S.; Antony, J.; Ehrlich, S.; Krieg, H. A Consistent and Accurate ab initio Parametrization of Density Functional Dispersion Correction (DFT-D) for the 94 Elements H-Pu. *J. Chem. Phys.* **2010**, *132*, 154104.
- (39) Grimme, S.; Ehrlich, S.; Goerigk, L. Effect of the Damping Function in Dispersion Corrected Density Functional Theory. *J. Comput. Chem.* **2011**, *32*, 1456–1465.
- (40) Morales-García, A.; Illas, F. Comprehensive Analysis of the Influence of Dispersion on Group-14 Rutile-type Solids. *Phys. Rev. Mater.* **2020**, *4*, No. 073601.
- (41) Blöchl, P. E. Projector Augmented-Wave Method. *Phys. Rev. B* **1994**, *50*, 17953–17979.
- (42) Kresse, G.; Joubert, D. From Ultrasoft Pseudopotentials to the Projector Augmented-Wave Method. *Phys. Rev. B* **1999**, *59*, 1758–1775.
- (43) Monkhorst, H. J.; Pack, J. D. Special Points for Brillouin-Zone Integrations. *Phys. Rev. B* **1976**, *13*, 5188–5192.
- (44) Morales-García, A.; Valero, R.; Illas, F. An Empirical, yet Practical Way To Predict the Band Gap in Solids By Using Density Functional Band Structure Calculations. *J. Phys. Chem. C* **2017**, *121*, 18862–18866.
- (45) Krukau, A. V.; Vydrov, O. A.; Izmaylov, A. F.; Scuseria, G. E. Influence of the Exchange Screening Parameter on the Performance of Screened Hybrid Functionals. *J. Chem. Phys.* **2006**, *125*, 224106.
- (46) Rajaji, V.; Dutta, U.; Sreeparvathy, P. C.; Sarma, S. C.; Sorb, Y. A.; Joseph, B.; Sahoo, S.; Peter, S. C.; Kanchana, V.; Narayana, C. Structural, Vibrational, and Electrical Properties of 1T-TiTe<sub>2</sub> Under Hydrostatic Pressure: Experiments and Theory. *Phys. Rev. B* **2018**, *97*, No. 085107.
- (47) Zhou, Y.; Chen, C.; Zhou, Y.; Chen, X.; Gu, C.; An, C.; Zhang, B.; Yuan, Y.; Wu, H.; Zhang, R.; Zhang, L.; Zhu, X.; Yang, X.; Yang, Z. Pressure-induced Evolution of Structural and Electronic Properties in TiTe<sub>2</sub>. *Phys. Rev. B* **2019**, *99*, 125104.
- (48) Hu, K.; Lian, J.; Zhu, L.; Chen, Q.; Xie, S.-Y. Prediction of Fe2P-type TiTe<sub>2</sub> Under Pressure. *Phys. Rev. B* **2020**, *101*, 134109.
- (49) Mora-Fonz, D.; Schön, J. C.; Prehl, J.; Woodley, S. M.; Catlow, C. R. A.; Shluger, A. L.; Sokol, A. A. Real and Virtual Polymorphism



- 689 of Titanium Selenide with Robust Interatomic Potentials. *J. Mater.*  
690 *Chem. A* **2020**, *8*, 14054.
- 691 (50) Yu, F.; Sun, J.-X.; Zhou, Y.-H. The High-pressure Phase  
692 Transition of TiS<sub>2</sub> from First-principles Calculations. *Solid State Sci.*  
693 **2010**, *12*, 1786.
- 694 (51) Léger, J. M.; Pereira, A. S.; Haines, J.; Jobic, S.; Brec, R. Phase  
695 Transformations of Polymeric CdI<sub>2</sub>-type IrTe<sub>2</sub> under high pressure. *J.*  
696 *Phys. Chem. Solids* **2000**, *61*, 27.
- 697 (52) Birch, F. Finite Elastic Strain of Cubic Crystals. *Phys. Rev.* **1947**,  
698 *71*, 809–824.
- 699 (53) Murnaghan, F. D. The Compressibility of Media under  
700 Extreme Pressures. *Proc. Nat. Acad. Sci.* **1944**, *30*, 244–247.
- 701 (54) Zhang, X.; Tan, Q. H.; Wu, J.-B.; Shi, W.; Tan, P. H. Review on  
702 the Raman Spectroscopy of Different Types of Layered Materials.  
703 *Nanoscale* **2016**, *8*, 6435–6450.
- 704 (55) Zhang, X.; Qiao, X.-F.; Shi, W.; Wu, J. B.; Jiang, D. S.; Tan, P.  
705 H. Phonon and Raman Scattering of Two-Dimensional Transition  
706 Metal Dichalcogenides from Monolayer, Multilayer to Bulk Material.  
707 *Chem. Soc. Rev.* **2015**, *44*, 2757–2785.
- 708 (56) Cingolani, A.; Lugarà, M.; Lévy, F. Resonance Raman  
709 Scattering in HfSe<sub>2</sub> and HfS<sub>2</sub>. *Phys. Scr.* **1988**, *37*, 389–391.
- 710 (57) Katkanant, V.; Kirby, R. D. Mixed-Crystal Lattice Dynamics of  
711 Hf<sub>x</sub>Ti<sub>1-x</sub>Se<sub>2</sub>. *Phys. Rev. B* **1989**, *40*, 1152–1158.
- 712 (58) Greenaway, D. L.; Nitsche, R. Preparation and Optical  
713 Properties of Group IV-VI<sub>2</sub> Chalcogenides Having the CdI<sub>2</sub>  
714 Structure. *J. Phys. Chem.* **1965**, *26*, 1445–1458.
- 715 (59) Gaiser, C.; Zandt, T.; Krapf, A.; Serverin, R.; Janowitz, C.;  
716 Manzke, R. Band-Gap Engineering with HfS<sub>x</sub>Se<sub>2-x</sub>. *Phys. Rev. B* **2004**,  
717 *69*, No. 075205.
- 718 (60) Guzman, D. M.; Strachan, A. Role of Strain on Electronic and  
719 Mechanical Response of Semiconducting Transition-Metal Dichalco-  
720 genide Monolayers: An ab-initio Study. *J. Appl. Phys.* **2014**, *115*,  
721 243701.